Journal of Magnetism and Magnetic Materials 563 (2022) 170018

Contents lists available at ScienceDirect

Journal of Magnetism and Magnetic Materials

journal homepage: www.elsevier.com/locate/jmmm

Research article

Probing magnetic anisotropy in Kagome antiferromagnetic Mn_3Ge with torque magnetometry

Y.S. Liu [a,b,c], H. Xiao [d], A.B. Yu [e], Y.F. Wu [a], K. Manna [f,g], Claudia Felser [f], C.M. Schneider [b,c], Hong-Yi Xie [a], T. Hu [a,*]

[a] Beijing Academy of Quantum Information Sciences, Beijing, 100193, China
[b] Fakultät für Physik, Universität Duisburg–Essen, D-47057 Duisburg, Germany
[c] Peter Grünberg Institute PGI-6, Forschungszentrum Jülich, D-52425 Jülich, Germany
[d] Center for High Pressure Science and Technology Advanced Research, Beijing, 100094, China
[e] State Key Laboratory of Functional Materials for Informatics, Shanghai Institute of Microsystem and Information Technology, Chinese Academy of Sciences, Shanghai 200050, China
[f] Max Planck Institute for Chemical Physics of Solids, Dresden, Germany
[g] Indian Institute of Technology- Delhi, Hauz Khas, New Delhi 110 016, India

ARTICLE INFO

Keywords:
Weyl semimetal
Torque magnetometry
Magnetic switching

ABSTRACT

We investigate the magnetic symmetry of the topological antiferromagnetic material Mn_3Ge by torque measurements. Below the Néel temperature, detailed angle-dependent torque measurements were performed on Mn_3Ge single crystals in directions parallel and perpendicular to the Kagome basal plane. The out-of plane torque data exhibit $\pm\sin\theta$ and $\sin 2\theta$ behaviors, of which the former results from the spontaneous ferromagnetism within the basal plane and the latter from the in- and out-of-plane susceptibility anisotropy. The reversible component of the in-plane torque exhibits $\sin 6\varphi$ behavior, revealing the six-fold symmetry of the in-plane magnetic free energy. Moreover, we find that the free energy minima are pinned to the direction of spontaneous ferromagnetism, which corresponds to the maxima of the irreversible component of the in-plane torque. We provide an effective spin model to describe the in-plane magnetic anisotropy. Our results demonstrate that the ground state of Mn_3Ge is described by the coexistence of a strong six-fold antichiral order and a weak ferromagnetic order induced by second-order spin anisotropy.

1. Introduction

The topological antiferromagnets, combining the characteristics of nontrivial topology and antiferromagnetism, arouse significant interests in modern spintronics [1,2]. Antiferromagnetic materials are ideal platforms for spintronics applications because of their low susceptibility to external magnetic fields and vanishing stray field. In addition, exceptional Berry curvatures of the electron bands in topological antiferromagnets can give rise to the intrinsic anomalous Hall effect [3], as strong as that observed in conventional ferromagnetic materials [4–7]. Recently, the Kagome-type noncollinear antiferromagnetic compounds Mn_3X, including the hexagonal compounds with X=Ge, Sn, and Ga, and the cubic compounds with X=Ir and Pt, have attracted intensive studies [8,9]. In particular, Mn_3Ge and Mn_3Sn were proposed to be antiferromagnetic Weyl semimetals [4,7,10–12]. A variety of intriguing phenomena were observed, such as large anomalous Hall effect [5,6,9,13–16], spin Hall effect [8,17,18], anomalous Nernst effect [19–22], and magneto-optical Kerr effect [23]. Imaging and writing magnetic domains via the anomalous Nernst effect has also been realized [24]. Recently, the all-electronically controlled antiferromagnetic magnetization switching without external field is realize in Mn_3Sn [25]. Among those compounds, Mn_3Ge has been found to exhibit a large intrinsic anomalous Hall effect even at room temperature and this effect is strongly anisotropic and can be switched with a small applied magnetic field [6,26].

These interesting transport properties are attributed to the peculiar magnetic patterns of the Mn spins. The unit cell of Mn_3Ge is hexagonal and can be described by the $P6_3/mmc$ space group with Mn and Ge on the $6h$ and 2c Wyckoff sites, respectively. The Mn atoms are arranged in a Kagome pattern, with two Kagome layers per unit cell stacked along the c axis with an in-plane displacement [See the inset of Fig. 1(b)]. Mn_3Ge is a noncollinear antiferromagnetic crystal with antichiral Mn-spin structure in the basal plane below the Néel temperature T_N ranging from 365 K to 400 K [6,27–32]. The resulting electron bands can support Weyl points that act as effective monopoles generating large Berry curvatures at the Fermi surface [4,33,34]. Nevertheless, the magnetic anisotropies of the Mn_3X family

* Corresponding author.
E-mail addresses: xiehy@baqis.ac.cn (H.-Y. Xie), hutao@baqis.ac.cn (T. Hu).

https://doi.org/10.1016/j.jmmm.2022.170018
Received 29 July 2022; Received in revised form 17 September 2022; Accepted 27 September 2022
Available online 3 October 2022

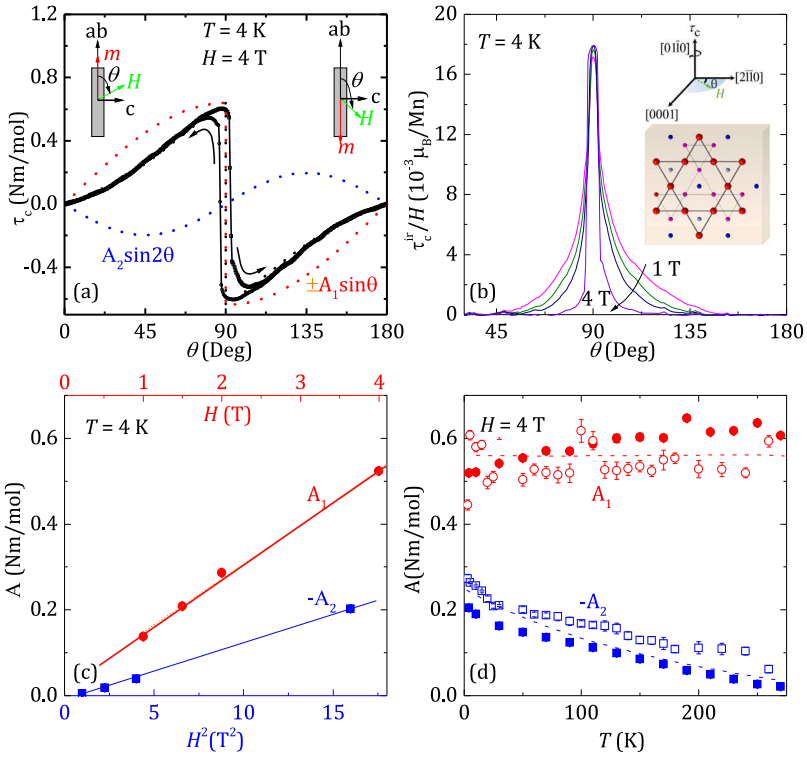

Fig. 1. Out-of plane torque $\tau_c(\theta)$ measurements. The experimental geometry is depicted in the inset of panel (b). (a) τ_c as a function of θ sweeping in anticlockwise (right arrow) and clockwise (left arrow) directions at $T = 4\,\mathrm{K}$ and $H = 4\,\mathrm{T}$. As defined in Eq. (1), the reversible torque $\tau_c^{re}(\theta)$ consists of two components A_1 (red dashed line) and A_2 (blue dashed line). (b) Normalized irreversible torque τ_c^{ir}/H as a function of θ for magnetic fields $1\,\mathrm{T} \le H \le 4\,\mathrm{T}$ at $T = 4\,\mathrm{K}$. (c) Coefficients A_1 (top axis and red symbols) and A_2 (bottom axis and blue symbols) as functions of H and H^2, respectively, at $T = 4\,\mathrm{K}$. (d) Coefficients A_1 (red symbols) and A_2 (blue symbols) as functions of temperature T at $H = 4\,\mathrm{T}$. The dash lines are guides to the eyes and the solid and hollow symbols are the results for the samples with the masses of 1.45 mg and 0.0157 mg, respectively.

have long been investigated and debated. The torque measurements in Mn_3Sn indicate a six-fold symmetry and another two-fold symmetry of the magnetic anisotropy [35]. While a near cubic symmetry of the anisotropy is found in noncollinear antiferromagnet $L1_2$-ordered Mn_3Ir, which is never found in ferromagnets [36–38]. In addition, an extremely strong second-order anisotropy appears in Mn_3Ir due to its frustrated triangular magnetic ground state [39]. For Mn_3Ge it was argued that no in-plane anisotropy energy exists up to four-fold terms [26,28,29], because the second- and the fourth-order anisotropy energies from each Mn site cancel out and cannot induce significant energy landscapes [40]. However, a weak in-plane ferromagnetic moment with nearly isotropic susceptibility is detected in Mn_3Ge [29,30]. The origin of this small ferromagnetism is not yet clarified and can be determined by either spin–orbit coupling effects [4,41,42] or the local spin anisotropy [40,43–45]. Besides, the magnetic anisotropy for fields applied along different crystallographic directions have not been thoroughly evaluated, despite of the availability of neutron diffraction studies [45,46].

In this work, we use torque magnetometry as a sensitive probe to investigate the macroscopic magnetic anisotropy in hexagonal Mn_3Ge single crystals and provide a theoretical analysis based on effective Hamiltonian expressed in terms of magnetic order parameters. Torque magnetometry is a highly sensitive tool to detect the magnetic anisotropy of materials. A finite torque, defined as $\boldsymbol{\tau} = \mathbf{m} \times \mathbf{H}$, arises as if the magnetization $\mathbf{m}$ is no longer collinear with the applied magnetic field $\mathbf{H}$. For a fixed rotation axis, the reversible component of the torque is the rotation-angle derivative of the thermodynamic free energy, i.e., $\tau(\theta) = -dF/d\theta$, while the irreversible component of the torque can be induced by the free energy minima acting as intrinsic pinning centers [47–49]. We introduce an effective spin model to analyze the observed magnetic anisotropy.

2. Experimental details

High-quality Mn_3Ge single crystals were synthesized by melting stoichiometric quantities of Mn and Ge elements using the Bridgman–Stockbarger technique [6]. The angle-dependent magnetic torques of Mn_3Ge were performed by using a piezoresistive torque magnetometer in the Quantum Design Physical Property Measurement System. The sample was mounted on the center of the torque-lever chip by applying a small amount of Apiezon N grease. The torsion can be detected by two piezoresistor grids on the legs of torque lever when the sample was applied under a magnetic field. The small resistance changes were measured by a Wheatstone bridge and compared to the calibrated chip prior to the measurement. The change of the resistance values are therefore converted into the torque signal with the unit of Nm. The experimental geometries for out-of plane and in-plane rotations are shown in the insets of Figs. 1(b) and 2(c), respectively.

3. Results and discussion

Fig. 1(a) shows the out-of-plane angle θ dependence of torque (τ_c) in anticlockwise (τ_c^+) and clockwise (τ_c^-) directions at $T = 4\,\mathrm{K}$ and $H = 4\,\mathrm{T}$. It is found that, when the magnetic field is nearly along the c axis ($\theta \approx 90°$), $\tau_c(\theta)$ switches to the opposite value and exhibits a large torque hysteresis loop in one angle-sweep circle. Such a hysteresis loop indicates magnetic pinning of a spontaneous ferromagnetic moment $\mathbf{m}$ within the basal plane. In fact, the $M(H)$ loop was previously measured with the magnetic field along with the basal plane and out-of plane [6]. It displays a tiny spontaneous magnetization of $0.005–0.006\mu_B$/Mn at 2 K within the basal plane, which is an order of magnitude larger than that in the out-of plane [6]. It is evident that the basal plane is the energetically most favored plane of spontaneous magnetic symmetry breaking dominated by the Dzyaloshinskii–Moriya interaction [28,30,32,45,46,50]. As sketched in the inset of Fig. 1(a), the ferromoment $\mathbf{m}$

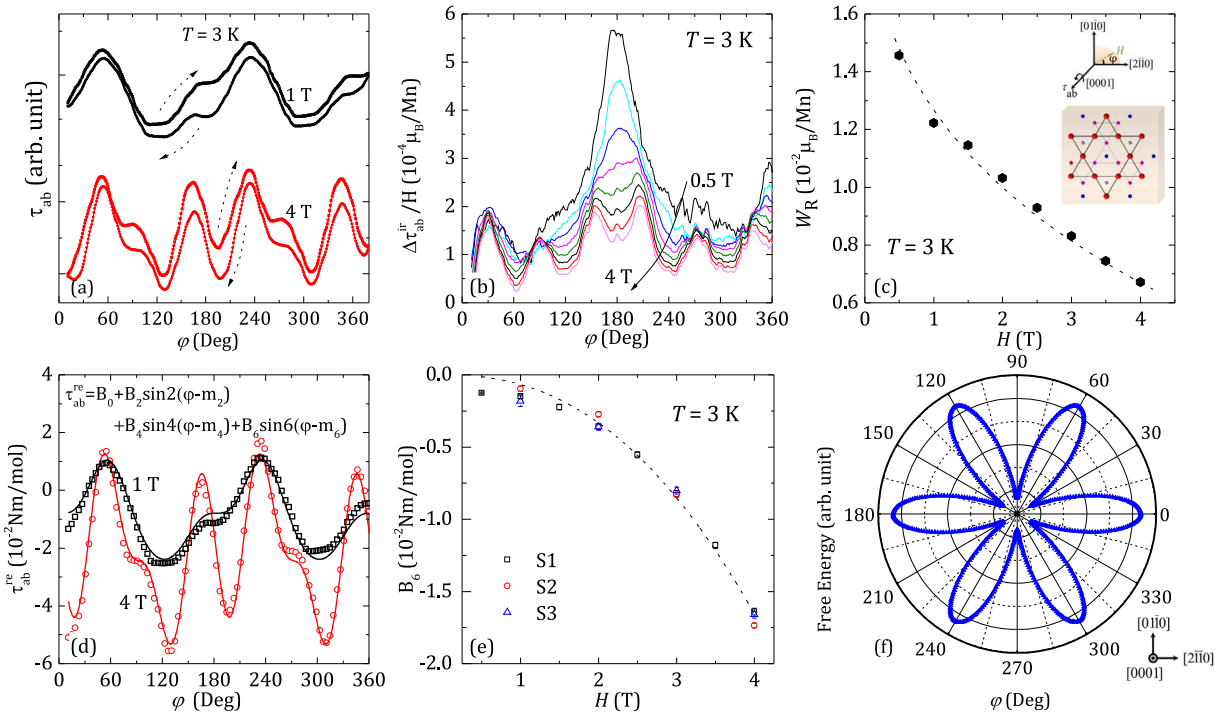

Fig. 2. In-plane torque $\tau_{ab}(\varphi)$ measurements. The experimental geometry is depicted in the inset of panel (c). (a) $\tau_{ab}(\varphi)$ as a function of φ sweeping in anticlockwise (right arrows) and clockwise (left arrows) directions at $T = 3\,\mathrm{K}$ and $H = 1\,\mathrm{T}$ (black lines) and $H = 4\,\mathrm{T}$ (red lines). (b) Normalized irreversible torque $\tau^{\mathrm{ir}}_{ab}/H$ as a function of φ for $0.5\,\mathrm{T} \le H \le 4\,\mathrm{T}$ with a step of $0.5\,\mathrm{T}$ at $T = 3\,\mathrm{K}$. (c) Rotation hysteresis W_{R} as a function of H. (d) Reversible torque $\tau^{\mathrm{re}}_{ab}(\varphi)$ for $H = 1\,\mathrm{T}$ (black square) and $H = 4\,\mathrm{T}$ (red circle) at $T = 3$ K. The solid lines are fitting results by using Eq. (2). (e) Coefficient B_6 as a function of H at $T = 4\,\mathrm{K}$. S_1 and S_2 indicate regular-shape samples of square cross section with masses of 5.9 mg and 3.1 mg, respectively, and S_3 indicates an irregular-shape sample with mass of 4.5mg. The dashed lines are the fitting results by using AH^n with $n = 2.3 \pm 0.1$. (f) Polar plot of the magnetic anisotropic free energy $F(\varphi)$ (blue line) obtained from the B_6 component of the reversible torque in (d).

flips within the basal plane as the in-plane component of the applied field goes to the opposite direction, which, therefore, results in a sign reverse of the torque about $\theta = 90°$. As shown in the inset of Fig. 1(b), we find that **m** is parallel to the $[2\bar{1}\bar{1}0]$ direction. Moreover, we estimate its amplitude m based on the irreversible torque $\tau_c^{\mathrm{ir}} \equiv \tau_c^{+} - \tau_c^{-} = 2\,mH$ at $\theta = 90°$. Fig. 1(b) shows the normalized irreversible torque $\tau_c^{\mathrm{ir}}(\theta)/H$ as a function of θ measured for $1\,\mathrm{T} \le H \le 4\,\mathrm{T}$. We find that $\tau_c^{\mathrm{ir}}(\theta = 90°)/H = 0.018\,\mu_{\mathrm{B}}$ and the value is field-independent. This gives $m = 0.009\,\mu_{\mathrm{B}}$/Mn, which is consistent with the spontaneous in-plane magnetization $0.007\,\mu_{\mathrm{B}}$/Mn observed in various studies [6,28,30].

The spontaneous ferromoment is also observed in the reversible component of the torque, i.e., $\tau_c^{\mathrm{re}} \equiv (\tau_c^{+} + \tau_c^{-})/2$. In Fig. 1(a), we fit $\tau_c^{\mathrm{re}}(\theta)$ data by the formula

$$\tau_c^{\mathrm{re}}(\theta) = \pm A_1 \sin\theta + A_2 \sin 2\theta. \tag{1}$$

Here, the A_1 component (the red dotted curve) results from the spontaneous ferromoment, which takes the positive sign "+ " for $0 < \theta < \pi/2$ and the negative sign "−" for $\pi/2 < \theta < \pi$, so that it changes suddenly at $\theta = \pi/2$. The A_2 component (the blue dotted curve) originates from the difference between the in-plane and out-of-plane susceptibilities. We show the field and temperature dependence of $A_{1,2}$ in Figs. 1(c) and 1(d).

In Fig. 1(c), we observe that A_1 increases linearly with H, which confirms a constant in-plane magnetic moment $m = A_1/H = 0.124 \pm 0.005\,\mathrm{Nm/mol/T}$ $(0.0075 \pm 0.0003\,\mu_{\mathrm{B}}/\mathrm{Mn})$, consistent with that found in the irreversible torque in Fig. 1(a). As shown in Fig. 1(d), m is temperature-independent up to $T \approx 275\,\mathrm{K}$, which is still far below the Néel temperature. On the other hand, from the A_2 component we can obtain the susceptibility anisotropy $\Delta\chi \equiv \chi_{ab} - \chi_c$, where χ_c and χ_{ab} are the out-of- and in-plane susceptibilities, respectively, because the field-induced magnetization produces a torque equal to $\frac{1}{2}\Delta\chi H^2 \sin 2\theta$ [51,52]. In Fig. 1(c), we show that A_2 is negatively proportional to H^2 and obtain $\Delta\chi = -0.0278\ \mathrm{m^3/mol}$ at $T = 4\,\mathrm{K}$, which is consistent with the previous studies [6,30]. Fig. 1(d) indicates that $\Delta\chi < 0$ in the temperature range below 275 K and tends to go to zero as the temperature increases. The low-temperature susceptibility anisotropy reflects the strength of the Dzyaloshinskii–Moriya interaction [43], while the high-temperature behavior $\chi_{ab} \to \chi_c$ ought to be the signal of suppression of magnetic anisotropy as the Néel temperature is approached from below. It is worthy to note that the data in Fig. 1(d) are taken from the two distinct samples with masses of 1.45 mg and 0.0157 mg, where the 0.0157 mg is derived from the torque signal since it is far too small to measure on an ordinary balance.

In Fig. 2(a), we show the in-plane angle φ dependence of the torque τ_{ab} in anticlockwise and clockwise directions at $T = 3\,\mathrm{K}$ and $H = 1\,\mathrm{T}$ and 4 T. We observe that $\tau_{ab}(\varphi)$ exhibits hysteresis at almost any angle, which signals magnetic pinning. Fig. 2(b) shows the normalized irreversible torque $\tau^{\mathrm{ir}}_{ab}/H$ as a function of φ for various field strengths ranging from 0.5 T to 4 T. We observe that $\tau^{\mathrm{ir}}_{ab}/H$ exhibits two peaks for $H < 1.5\,\mathrm{T}$ and six peaks at $\varphi_n = 30° + (n-1) \times 60°$ $(1 \le n \le 6)$ for $H > 1.5\,\mathrm{T}$. The six peaks originate from the six-fold in-plane magnetic anisotropy due to the crystal field effect [see Eq. (A.3) and Ref. [53]]. In Fig. 2(c), we show the rotational hysteresis, define by the area of the hysteresis loop $W_{\mathrm{R}} \equiv \int_0^{2\pi} \tau^{\mathrm{ir}}_{ab}(\varphi)\,d\varphi$ and giving twice the energy lost in rotating the magnetization, as a function of magnetic field. The high-field rotational hysteresis reveals the existence of the unidirectional anisotropy due to the coupling between ferromagnetic and antiferromagnetic orders [54,55], which occurs in parallel with the exchange bias in the magnetization curves of Mn_3Ge [32].

In Fig. 2(d), we fit the reversible torque $\tau^{\mathrm{re}}_{ab}(\varphi)$ using the formula

$$\tau^{\mathrm{re}}_{ab}(\varphi) = B_0 + B_2 \sin[2(\varphi - m_2)] + B_4 \sin[4(\varphi - m_4)] + B_6 \sin[6(\varphi - m_6)]. \tag{2}$$

The fitting result of B_6 is shown in Fig. 2(e). Besides the sample S1 discussed above, Fig. 2(e) also includes the data from the samples S2 and S3, where the black and red hollow symbols are for regular-shape

samples of square cross section with masses of 5.9 mg and 3.1 mg, respectively, and the blue symbols for irregular-shape sample with mass of 4.5 mg. We observe that B_6 is negative and sample-independent and its magnitude increases with the increase of H exhibiting the H^n dependent behavior with $n = 2.3 \pm 0.1$ as the dash line shown in Fig. 2(e). This observation suggests the intrinsic six fold in-plane anisotropy properties of Mn_3Ge and rules out extrinsic effects such as magnetoelastic forces. We note that the fitting result of $B_{0,2,4}$ is not included in Fig. 2(e), because these components are plausibly extrinsic: B_0 comes from the background of torque magnetometer, and $B_{2,4}$ are different in magnitude for the three samples and likely induced by the artificial magnetoelastic anisotropy, which cannot indicate the intrinsic magnetization with respect to the crystallographic axes [56,57].

In order to further investigate the six-fold symmetry of the magnetic anisotropy in Mn_3Ge, we convert the reversible torque into magnetic free energy by the definition $F(\varphi) = -\int \tau^{\rm re}_{ab}(\varphi)\, d\varphi$ up to a constant. In Fig. 2(f), we show the free energy (blue line) and the related crystal orientation of Mn_3Ge samples (red line) in the polar coordinates. We find free energy minima $\varphi_n = 30° + (n-1) \times 60°$ $(1 \le n \le 6)$, which coincide with the peaks of the irreversible torques at high field as shown in Fig. 2(b). Not as a surprise, the symmetry of free energy respecting the Kagome lattice is consistent with the symmetry obtained by the neutron diffraction studies [45,46]. This confirms that the magnetic easy axis points aiming the $[01\bar{1}0]$ direction as shown in the insets of Figs. 1(b) and 2(c).

It has been suggested that the ground-state magnetic phase of Mn_3Ge is described by two in-plane vector orders, i.e., the antichiral (AC) order $\mathbf{A} = (A_x, A_y)$ [Fig. 3(c)] and the ferromagnetic (FM) order $\mathbf{M} = (M_x, M_y)$ [Fig. 3(d)], which are transformed according to the irreducible representation E_{1g} of the D_{6h} group [45,46]. The in-plane magnetic anisotropy can be characterized by the effective Hamiltonian written in the polar coordinates $\mathbf{M} = M(\cos\alpha, \sin\alpha)$ and $\mathbf{A} = A(\cos\beta, \sin\beta)$ as

$$\begin{aligned}\mathcal{H} = &-(J/6)A^2 + [C_6^0 + C_6^6\cos(6\beta)]A^6 + (J/3)M^2 \\ &+ [C_6^0 + C_6^6\cos(6\alpha)]M^6 - 2C_2^2 AM\cos(\alpha-\beta) \\ &- 2\, g\mu_{\rm B} HM\cos(\varphi-\alpha),\end{aligned} \tag{3}$$

where $J > 0$ is the Heisenberg exchange energy, $C_6^{0,6}$ and C_2^2 are anisotropy energies, $H(\cos\varphi, \sin\varphi)$ is an applied Zeeman field, and g and $\mu_{\rm B}$ denote the Landé g-factor and Bohr magneton, respectively. We note that Eq. (3) in the absence of the Zeeman term and M^6 term has been introduced in Ref. [45]. We present the derivation of Eq. (3) based on the crystal electric field theory in Appendix. Minimizing the energy (3) with respect to (M, A, α, β), one can obtain the ground and metastable states.

The signs of the anisotropy energies $C_6^{0,6}$ and C_2^2 can be fixed by our torque measurements. (i) The relation $C_6^0 > |C_6^6|$ must be satisfied as the Hamiltonian (3) should process a well-defined ground state. Otherwise, for $C_6^0 < |C_6^6|$, the ground state prefers infinitely large AC and FM orders. (ii) In the presence of the Zeeman field, the in-plane torque $\tau_{ab} = 3C_6^6(A^6\sin 6\beta + M^6\sin 6\alpha)$, where (A, M, α, β) take the values of metastable states. In large-field limit $g\mu_B H \gg C_6^6(A^6 + M^6)$, the reversible torque $\tau^{\rm re}_{\rm ab} \sim C_6^6\sin(6\varphi)$. According to the extrema of the free energy in Fig. 2(f), we can fix $C_6^6 > 0$. As a consequence, the ground state prefers A_y $(\beta = \pi/2)$ order in Fig. 3(c). (iii) In the absence of Zeeman field, the observed FM order in Fig. 1 indicates finite AC–FM coupling C_2^2, because the minima of the Hamiltonian (3) occurs at $M = 0$ if $C_2^2 = 0$. Moreover, since the FM order is along the $[01\bar{1}0]$ direction, i.e., M_y configuration in Fig. 3(d), we conclude that $C_2^2 > 0$. Summarizing the conclusions of (i)-(iii), we obtain

$$C_6^0 > C_6^6 > 0, \quad C_2^2 > 0. \tag{4}$$

The ground-state orders M_y and A_y are consistent with the observations in Refs. [45] and [46].

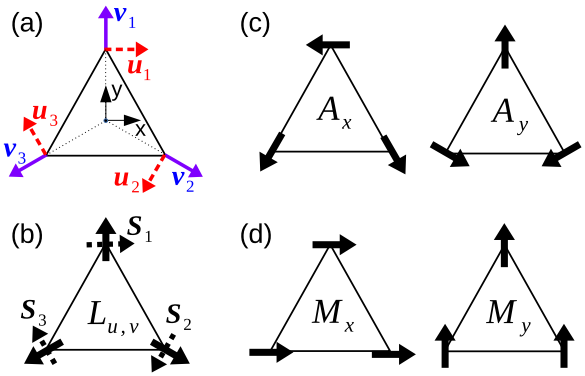

Fig. 3. Spin configurations corresponding to the order parameters in Eq. (A.2). (a) Local orthogonal easy axes $\mathbf{u}_{1,2,3}$ (red) and $\mathbf{v}_{1,2,3}$ (blue). We note that $\mathbf{v}_1$ corresponds to $[01\bar{1}0]$ direction in Figs. 1 and 2. (b) Chiral orders L_u (solid) and L_v (dotted). (c) Antichiral order **A**. (d) Ferromagnetic order **M**. Experimental data in Figs. 1(a) and 2(f) indicate that the ground state prefers the coexistence of A_y and M_y.

The rotational hysteresis W_R in Fig. 2(c) equals to twice the energy difference between meta-stable states at the discontinuous jumps as the sample rotating. Without the six-fold anisotropy $C_6^6 = 0$, the in-plane torque is reversible and the rotational hysteresis vanishes $W_R = 0$. On the other hand, in analogy to the materials with FM–anti-FM interfaces [54,55], the persistence of W_R at high Zeeman fields should demonstrate finite FM–AC coupling, since for FM order alone W_R exists only in a narrow field range. Therefore, the observed W_R ought to be attributed to the combination effect of the six-fold anisotropy and the AC–FM coupling. However, obtaining W_R as a function of C_6^6 and C_2^2 requires a full meta-stability analysis of the Hamiltonian in Eq. (3) and deserves a separate study.

Moreover, from Eq. (3) we can obtain the amplitudes of the ground-state order parameters

$$M = 3C_2^2 A/J, \quad A = \left(J/18\Delta_6\right)^{1/4}, \tag{5}$$

where $\Delta_6 = C_6^0 - C_6^6 > 0$. Therefore, the AC-induce FM order is weak $M/A \sim C_2^2/J \ll 1$, since the anisotropy energies are much smaller the Heisenberg exchange energy. From our experimental data, we estimate the equilibrium orders $M = 3 \times 0.0075/g$ and $A = 3 \times 2.2/g$, where the factor "3" captures the number of spins. Combining the expression of the susceptibility anisotropy $\Delta\chi = 8\sqrt{3}g^2\mu_{\rm B}^2 D/(3J^2)$ [43] and Eq. (5), we estimate the relevant energy parameters in Eq. (3), $J = 22.4\,$meV, $D = -2.54\,$meV, $C_2^2 = 2.5 \times 10^{-2}\,$meV, $\Delta_6 = 1.0 \times 10^{-2}\,$meV, where we have taken $g = 2$ and the value of J in Ref. [43].

We would like to point out that comparing the characteristic parameters of the Mn3X family measured by different methods is never easy. We realize that one of the most annoying obstacles is that various spin models were introduced to fit experimental data. For example, for investigating Mn3Ge distinct spin models were introduced in Ref. [40] [Cable et al. PRB 48, 6259 (1993)] and in Ref. [45] [Soh et al. PRB 101, 140411 (2020)], and, unfortunately, the basal-plane characteristic parameters were not well established. In our work, we proposed that the Hamiltonian given by Eq. (3) is a "minimal" model that could describe the basal-plane magnetic anisotropy of Mn3Ge and the parameters can be estimated from our torque data.

4. Summary

In summary, we investigated the anisotropic magnetic properties of the antiferromagnet Mn_3Ge by torque magnetometry. A spontaneous ferromoment of $m = (7.5 \pm 0.3) \times 10^{-3}\,\mu_{\rm B}$/Mn is found to arise within the Kagome basal plane in $[01\bar{1}0]$ direction [Fig. 1(b)]. Furthermore, in-plane magnetic free energy possesses a six fold symmetry with the minima at $\varphi_n = 30° + (n-1) \times 60°$ $(1 \le n \le 6)$. These minima

weakly pin the spontaneous ferromoment and cause the maxima of irreversible in-plane torque. Exploiting an effective Hamiltonian we estimated the values of various coupling energies, and demonstrate that the ground state of Mn_3Ge is characterized by a strong AC order "ferromagnetically" coupling to a weak AC-order-induced FM order with unidirectional anisotropy along $[01\bar{1}0]$ axis. The two- and four-fold in-plane symmetries cannot been determined. For other hexagonal compounds as $Mn_3(Sn, Ga)$, one may consider the two- or four-fold anisotropies by introducing extra crystal electric field terms in Eq. (A.1) and a through study needs intensive numerical analysis.

Declaration of competing interest

The authors declare that they have no known competing financial interests or personal relationships that could have appeared to influence the work reported in this paper.

Data availability

Data will be made available on request.

Acknowledgments

T.H. acknowledge the support of NSFC Grant No. 11574338. The work of H.-Y.X. was supported by NSFC under Grant No. 12074039. H.X. acknowledge the support of NSAF Grant No. U1530402. K.M. and C.F. acknowledges financial support by European Research Council (ERC) Advanced Grant No. 742068 ("TOPMAT"), Deutsche Forschungsgemeinschaft (DFG) under SFB 1143 (Project No. 247310070) and Würzburg-Dresden Cluster of Excellence on Complexity and Topology in Quantum Matter-ct.qmat (EXC 2147, project no. 39085490). K.M. acknowledges Max Plank Society for the funding support under Max Plank–India partner group project and Board of Research in Nuclear Sciences (BRNS) under 58/20/03/2021-BRNS/37084/ DAE-YSRA.

Appendix. In-plane anisotropic Hamiltonian

In Mn_3X family the presence of the AC order reduces the magnetic symmetry from hexagonal D_{6h} to rhombic D_{2h} and the FM order furthermore reduces D_{2h} to monoclinic C_{2h} [40]. Assuming a uniform spin configuration respecting the translation and inversion symmetries, we consider the effective triple-spin Hamiltonian describing the energy per unit cell [43,45,46],

$$\mathcal{H} = J\sum_{\langle jk\rangle}\mathbf{S}_j\cdot\mathbf{S}_k + D\sum_{\langle jk\rangle}\hat{\mathbf{z}}\cdot(\mathbf{S}_j\times\mathbf{S}_k) + \sum_{l=1}^{3}\sum_{m=-l}^{l}C_{2l}^{2m}T_{2l}^{2m} - 2g\mu_B\mathbf{H}\cdot\sum_j\mathbf{S}_j, \tag{A.1}$$

where $J > 0$ is the sum of the Heisenberg exchanges, which favors noncollinear antiferromagnetic orders [Figs. 3(b) and 3(c)], $D < 0$ is the Dzyaloshinskii–Moriya (DM) interaction mediated by the spin–orbit coupling that aligns the spins in a 120° structure in the ab plane and favors the antichiral order [Fig. 3(c)], C_{2l}^{2m} represents the crystal field energy respecting the C_{2h} symmetry, and $\mathbf{H}$ is the applied magnetic field with g denoting the Landé g factor. In Eq. (A.1), the crystal field tensors T_{2l}^{2m} are defined by the Stevens operators O_{2l}^{2m} [58]: $T_{2l}^{2m} \equiv 3^{2l-1}\sum_{j=1}^{3}O_{2l}^{2m}(\mathbf{S}_j)$ and $O_{2l}^{0}(\mathbf{S}) = \mathbf{S}^{2l}$, $O_{2l}^{2l}(\mathbf{S}) = (S_+^{2l} + S_-^{2l})/2$, $O_{2l}^{-2l}(\mathbf{S}) = (S_+^{2l} - S_-^{2l})/(2i)$, $O_{2l}^{\pm 2m}(\mathbf{S}) = \mathbf{S}^{2l-2m}O_{2m}^{\pm 2m}(\mathbf{S})$ with $1 \le m \le l-1$, where $S_{j,\pm} \equiv (\mathbf{u}_j \pm i\mathbf{v}_j)\cdot\mathbf{S}_j$ is defined with respect to the local easy axes $\mathbf{u}_j = (\cos[2\pi(j-1)/3], \sin[2\pi(j-1)/3])$ and $\mathbf{v}_j = (\sin[2\pi(j-1)/3], -\cos[2\pi(j-1)/3])$, as shown in Fig. 3(a).

We parameterize the in-plane spins by six order parameters [45]

$$L_u = \sum_{j=1}^{3}\mathbf{u}_j\cdot\mathbf{S}_j, \quad L_v = \sum_{j=1}^{3}\mathbf{v}_j\cdot\mathbf{S}_j, \quad \mathbf{M} = \sum_{i=1}^{3}\mathbf{S}_i,$$

$$A_x = -(\mathbf{u}_1\cdot\mathbf{S}_1 + \mathbf{u}_2\cdot\mathbf{S}_3 + \mathbf{u}_3\cdot\mathbf{S}_2),$$
$$A_y = \mathbf{v}_1\cdot\mathbf{S}_1 + \mathbf{v}_2\cdot\mathbf{S}_3 + \mathbf{v}_3\cdot\mathbf{S}_2, \tag{A.2}$$

where the chiral orders L_u, L_v [Fig. 3(b)], and the AC order $\mathbf{A}$ [Figs. 3(c)] and the FM order $\mathbf{M}$ [Figs. 3(d)] are transformed according to the irreducible representations B_{1g}, B_{2g}, and E_{1g} of the D_{6h} group, respectively. In the polar coordinates $\mathbf{M} = M(\cos\alpha, \sin\alpha)$, $\mathbf{A} = A(\cos\beta, \sin\beta)$, and $\mathbf{H} = H(\cos\varphi, \sin\varphi)$, the Hamiltonian (A.1) reads

$$\mathrm{H} = aA^2 + bA^4 + c(6\beta)A^6 + dM^2 + bM^4 + c(6\alpha)M^6 + \sum_{k=1}^{3}\sum_{l=1}^{2k-1}f_{2k-l,l}(\alpha,\beta)A^{2k-l}M^l - 2\,g\mu_B H M\cos(\varphi-\alpha), \tag{A.3}$$

with the coefficients

$$\begin{aligned}
&a = -J/6,\ b = C_4^0,\ d = J/3,\ c(6\beta) = C_6^0 + C_6^6\cos 6\beta,\\
&f_{1,1}(\alpha,\beta) = -2C_2^2\cos(\alpha-\beta),\\
&f_{1,3}(\alpha,\beta) = -3C_4^2\cos(\alpha-\beta),\\
&f_{1,5}(\alpha,\beta) = -4C_6^2\cos(\alpha-\beta) - C_6^4\cos(5\alpha+\beta),\\
&f_{2,2}(\alpha,\beta) = 4C_4^0 + 6C_4^4\cos(2\alpha-2\beta),\\
&f_{2,4}(\alpha,\beta) = 9C_6^0 + C_6^2\cos(4\alpha+2\beta) + 10C_6^4\cos(2\alpha-2\beta),\\
&f_{3,3}(\alpha,\beta) = -2C_6^0\cos(3\alpha+3\beta) - 12C_6^2\cos(\alpha-\beta)\\
&\qquad\qquad - 20C_6^6\cos(3\alpha-3\beta),
\end{aligned} \tag{A.4}$$

and $f_{l,m}(\alpha,\beta) = f_{m,l}(\beta,\alpha)$.

Two simplifications have been introduced in (A.3): (i) We have taken $L_{u,v} = 0$, since no chiral orders have been observed in Mn_3Ge [45,46]. (ii) We have applied the energy hierarchy $J \gg |D| \gg |C_l^m| \gg |C_l^{-m}|$ for $m > 0$. According to the crystal field theory [58], D_{6h} symmetry only involves $C_{2,4,6}^0$ and C_6^6 terms; The AC order reduces D_{6h} symmetry to D_{2h}, which in addition involves $C_{2,4,6}^2$ and $C_{4,6}^4$ terms. The FM order reduces D_{2h} symmetry to C_{2h}, which furthermore involves $C_{2,4,6}^{-2}$, $C_{4,6}^{-4}$, and C_6^{-6}. For weak FM order in Mn_3Ge, we expect weak C_{2h} parameters, i.e., $|C_l^m| \gg |C_l^- m|$. Finally, it was argued that no in-plane anisotropy energy exists up to four-fold terms [26,28,29,40] in Mn_3Ge, so that we neglect the fourth order term $C_4^0 = 0$ and keep only the lowest-order AC–FM coupling term C_2^2. Thus the Hamiltonian (A.3) is simplified to Eq. (3).

References

[1] T. Jungwirth, X. Marti, P. Wadley, J. Wunderlich, Nature Nanotechnol. 11 (2016) 231.
[2] V. Baltz, A. Manchon, M. Tsoi, T. Moriyama, T. Ono, Y. Tserkovnyak, Rev. Modern Phys. 90 (2018) 015005.
[3] N. Nagaosa, J. Sinova, S. Onoda, A.H. MacDonald, N.P. Ong, Rev. Modern Phys. 82 (2010) 1539.
[4] J. Kübler, C. Felser, Europhys. Lett. 108 (2014) 67001.
[5] S. Nakatsuji, N. Kiyohara, T. Higo, Nature 527 (2015) 212.
[6] A.K. Nayak, J.E. Fischer, Y. Sun, B. Yan, J. Karel, A.C. Komarek, C. Shekhar, N. Kumar, W. Schnelle, J. Kübler, C. Felser, S.S. Parkin, Sci. Adv. 2 (2016) e1501870.
[7] J. Kübler, C. Felser, Europhys. Lett. 120 (2018) 47002.
[8] Y. Zhang, Y. Sun, H. Yang, J. Ž, S.P. Parkin, C. Felser, B. Yan, Phys. Rev. B 95 (2017) 075128.
[9] J. Mukherjee, T.S. Suraj, H. Basumatary, K. Sethupathi, K.V. Raman, Phys. Rev. Mater. 5 (2021) 014201.
[10] K. Kuroda, T. Tomita, M.-T. Suzuki, C. Bareille, A. Nugroho, P. Goswami, M. Ochi, M. Ikhlas, M. Nakayama, S. Akebi, et al., Nature Mater. 16 (2017) 1090.
[11] H. Yang, Y. Sun, Y. Zhang, W.-J. Shi, S.S. Parkin, B. Yan, New J. Phys. 19 (2017) 015008.
[12] T. Chen, T. Tomita, S. Minami, M. Fu, T. Koretsune, M. Kitatani, I. Muhammad, D. Nishio-Hamane, R. Ishii, F. Ishii, R. Arita, S. Nakatsuji, Nature Commun. 12 (2021) 572.
[13] H. Iwaki, M. Kimata, T. Ikebuchi, Y. Kobayashi, K. Oda, Y. Shiota, T. Ono, T. Moriyama, Appl. Phys. Lett. 116 (2020) 022408.
[14] Z. Liu, Y. Zhang, G. Liu, B. Ding, E. Liu, H.M. Jafri, Z. Hou, W. Wang, X. Ma, G. Wu, Sci. Rep. 7 (2017) 1.
[15] C. Sürgers, Nat. Electron. 1 (2018) 154.

[16] Z. Liu, H. Chen, J. Wang, J. Liu, K. Wang, Z. Feng, H. Yan, X. Wang, C. Jiang, J. Coey, et al., Nat. Electron. 1 (2018) 172.
[17] M. Kimata, H. Chen, K. Kondou, S. Sugimoto, P.K. Muduli, M. Ikhlas, Y. Omori, T. Tomita, A.H. MacDonald, S. Nakatsuji, et al., Nature 565 (2019) 627.
[18] W. Zhang, W. Han, S.-H. Yang, Y. Sun, Y. Zhang, B. Yan, S.S. Parkin, Sci. Adv. 2 (2016) e1600759.
[19] M. Ikhlas, T. Tomita, T. Koretsune, M.-T. Suzuki, D. Nishio-Hamane, R. Arita, Y. Otani, S. Nakatsuji, Nat. Phys. 13 (2017) 1085.
[20] D. Hong, N. Anand, C. Liu, H. Liu, I. Arslan, J.E. Pearson, A. Bhattacharya, J. Jiang, Phys. Rev. Mater. 4 (2020) 094201.
[21] C. Wuttke, F. Caglieris, S. Sykora, F. Scaravaggi, A.U. Wolter, K. Manna, V. Süss, C. Shekhar, C. Felser, B. Büchner, et al., Phys. Rev. B 100 (2019) 085111.
[22] L. Xu, X. Li, X. Lu, C. Collignon, H. Fu, J. Koo, B. Fauqué, B. Yan, Z. Zhu, K. Behnia, Sci. Adv. 6 (2020) eaaz3522.
[23] M. Wu, H. Isshiki, T. Chen, T. Higo, S. Nakatsuji, Y. Otani, Appl. Phys. Lett. 116 (2020) 132408.
[24] H. Reichlova, T. Janda, J. Godinho, A. Markou, D. Kriegner, R. Schlitz, J. Zelezny, Z. Soban, M. Bejarano, H. Schultheiss, et al., Nature Commun. 10 (2019) 1.
[25] Y. Deng, X. Liu, Y. Chen, Z. Du, N. Jiang, C. Shen, E. Zhang, H. Zheng, H.-Z. Lu, K. Wang, National Science Review (2022) http://dx.doi.org/10.1093/nsr/nwac154.
[26] N. Kiyohara, T. Tomita, S. Nakatsuji, Phys. Rev. A 5 (2016) 064009.
[27] T. Ohoyama, J. Phys. Soc. Japan 16 (1961) 1995.
[28] T. Nagamiya, S. Tomiyoshi, Y. Yamaguchi, Solid State Commun. 42 (1982) 385.
[29] S. Tomiyoshi, Y. Yamaguchi, T. Nagamiya, J. Magn. Magn. Mater. 31 (1983) 629.
[30] N. Yamada, H. Sakai, H. Mori, T. Ohoyama, Physica B+ C 149 (1988) 311.
[31] P. Brown, V. Nunez, F. Tasset, J. Forsyth, P. Radhakrishna, J. Phys.: Condens. Matter 2 (1990) 9409.
[32] J. Qian, A. Nayak, G. Kreiner, W. Schnelle, C. Felser, J. Phys. D: Appl. Phys. 47 (2014) 305001.
[33] Z. Fang, N. Nagaosa, K.S. Takahashi, A. Asamitsu, R. Mathieu, T. Ogasawara, H. Yamada, M. Kawasaki, Y. Tokura, K. Terakura, Science (2003) 92, 302.
[34] L. Šmejkal, T. Jungwirth, J. Sinova, Physica Status Solidi (RRL)–Rapid Research Letters 11 (2017) 1700044.
[35] T. Duan, W. Ren, W. Liu, S. Li, W. Liu, Z. Zhang, Appl. Phys. Lett. (2015) 082403, 107.
[36] S. Jenkins, R.W. Chantrell, T.J. Klemmer, R.F. Evans, Phys. Rev. B (2019) 220405, 100.
[37] G. Vallejo-Fernandez, L. Fernandez-Outon, K. O'Grady, Appl. Phys. Lett. (2007) 212503, 91.
[38] H. Chen, T.-C. Wang, D. Xiao, G.-Y. Guo, Q. Niu, A.H. MacDonald, Phys. Rev. B (2020) 104418, 101.
[39] L. Szunyogh, B. Lazarovits, L. Udvardi, J. Jackson, U. Nowak, Phys. Rev. B (2009) 020403, 79.
[40] J. Cable, N. Wakabayashi, P. Radhakrishna, Phys. Rev. B (1993) 6159, 48.
[41] K. Manna, Y. Sun, L. Muechler, J. Kübler, C. Felser, Nat. Rev. Mater. (2018) 244, 3.
[42] B. Nyári, A. Deák, L. Szunyogh, Phys. Rev. B (2019) 144412, 100.
[43] J. Liu, L. Balents, Phys. Rev. Lett. (2017) 087202, 119.
[44] S. Dasgupta, O. Tchernyshyov, 102 (2020) 144417.
[45] J.-R. Soh, F. de Juan, N. Qureshi, H. Jacobsen, H.-Y. Wang, Y.-F. Guo, A. Boothroyd, Phys. Rev. B (2020) 140411, 101.
[46] Y. Chen, J. Gaudet, S. Dasgupta, G. Marcus, J. Lin, T. Chen, T. Tomita, M. Ikhlas, Y. Zhao, W. Chen, et al., Phys. Rev. B 102 (2020) 054403.
[47] H. Xiao, T. Hu, C. Almasan, T. Sayles, M. Maple, Phys. Rev. B (2006) 184511, 73.
[48] T. Hu, H. Xiao, P. Gyawali, H. Wen, C. Almasan, Phys. Rev. B (2012) 134516, 85.
[49] M. Nauman, D.H. Kiem, S. Lee, S. Son, J.-G. Park, W. Kang, M.J. Han, Y. Jo, 2D Materials 8 (2021) 035011.
[50] S. Tomiyoshi, Y. Yamaguchi, J. Phys. Soc. Japan 51 (1982) 2478.
[51] M. Herak, D. Žilić, D.M. Č, H. Berger, Phys. Rev. B (2015) 174436, 91.
[52] Y. Hong, Y. Jo, H.Y. Choi, N. Lee, Y.J. Choi, W. Kang, Phys. Rev. B (2016) 094406, 93.
[53] H. Fujita, Phys. Status Solidi (RRL)–Rapid Res. Lett. 11 (2017) 1600360.
[54] W.H. Meiklejohn, C.P. Bean, Phys. Rev. (1957) 904, 105.
[55] J. Nogués, I.K. Schuller, J. Magn. Magn. Mater. 192 (1999) 203.
[56] E. Gomonay, V. Loktev, Phys. Solid State 47 (2005) 1755.
[57] H.V. Gomonay, V.M. Loktev, Phys. Rev. B 75 (2007) 174439.
[58] E. Bauer, M. Rotter, in: E. Belin-Ferré (Ed.), Properties and Applications of Complex Intermetallics, World Scientific, Singapore, 2009, pp. 183–248.